

Humans as a Calibration Pattern: Dynamic 3D Scene Reconstruction from Unsynchronized and Uncalibrated Videos

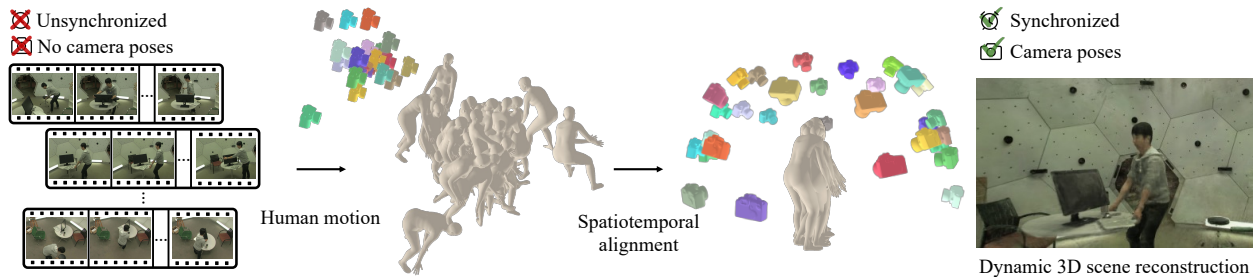
Changwoon Choi^{1*}Jeongjun Kim¹Geonho Cha²Minkwan Kim¹Dongyoon Wee²Young Min Kim^{1†}¹Seoul National University ²NAVER Cloud

Figure 1. We propose an approach to reconstruct dynamic 3D scenes from unsynchronized and uncalibrated videos. We exploit human motion as a calibration pattern to align time offsets and camera poses.

Abstract

Recent works on dynamic neural field reconstruction assume input from synchronized multi-view videos with known poses. These input constraints are often unmet in real-world setups, making the approach impractical. We demonstrate that unsynchronized videos with unknown poses can generate dynamic neural fields if the videos capture human motion. Humans are one of the most common dynamic subjects whose poses can be estimated using state-of-the-art methods. While noisy, the estimated human shape and pose parameters provide a decent initialization for the highly non-convex and under-constrained problem of training a consistent dynamic neural representation. Given the sequences of pose and shape of humans, we estimate the time offsets between videos, followed by camera pose estimations by analyzing 3D joint locations. Then, we train dynamic NeRF employing multiresolution grids while simultaneously refining both time offsets and camera poses. The setup still involves optimizing many parameters, therefore, we introduce a robust progressive learning strategy to stabilize the process. Experiments show that our approach achieves accurate spatiotemporal calibration and high-quality scene reconstruction in challenging conditions. [Project page](#)

*Work started during Changwoon’s internship at NAVER.

†Young Min Kim is the corresponding author.

1. Introduction

Recent advances in neural radiance fields (NeRF) have been extended into obtaining dynamic scenes of any topology [30] with small memory consumption [5, 8] using video inputs. However, even with a series of regularization techniques, obtaining a dynamic 3D volume with video inputs is a highly under-constrained problem and often suffers from instability and convergence problems. The claimed success of dynamic NeRF assumes either unrealistic movements of a monocular camera that can emulate a multi-view setup [9] or perfectly calibrated and synchronized multi-view inputs. Such input observations cannot be achieved in casual setups. Time synchronization often relies on hard-wired devices [10, 14] or needs additional cues [6] (e.g., sound peak). Pose estimation methods struggle in scenes with textureless area or repetitive structure, as shown in Fig. 2. Furthermore, it becomes more challenging if scenes are dynamic and videos are not synchronized.

We aim to allow training dynamic NeRF from a set of casually captured real-world videos of a shared event, such as a sports game or a concert, which only can be collected later. In other words, we reconstruct photorealistic 4D scenes from *unsynchronized* multi-view videos with *unknown camera poses*. We need strong priors to tackle this challenging problem with high degrees of freedom. We focus on *humans*, one of the most common dynamic objects in scenes. Human pose estimation in computer vision has progressed

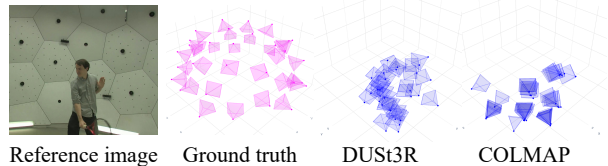


Figure 2. Both transformer-based method DUST3R [40] and SfM library COLMAP [36] fail to recover correct camera poses.

rapidly and now demonstrates a reliable performance even in general images or videos. We consider an estimated human parameter a robust mid-level representation to deduce the relationship between unsynchronized videos. Namely, we exploit human motion as a calibration pattern to estimate both time offsets and camera poses.

We first find the time offsets using the sequence of human shape and pose parameters estimated from individual videos. We can obtain a robust estimation of time offsets by enforcing global consistency in the sequence of motions with exhaustive pairwise scores. Specifically, we consider the detected parametric model of a human as a time series whose feature vector is the pose and shape parameters. We apply dynamic time warping (DTW) between every pair of videos to compute a constant offset to minimize the overall discrepancy in the explicit 3D joint positions and record the associated cost value. The pairwise values are stored within a matrix, from which we find a global sequence alignment with the overall minimum costs.

Even with slight misalignments, NeRF results can degrade significantly. Previous works propose optimizing camera poses jointly with the static scene, which only works with a good initialization point. Our initialization comes from the alignment of human motions, by applying Procrustes analysis on aggregated 3D joint positions across all frames. Note that we estimate transformation that maps camera coordinate to coherent global coordinate, so that we can estimate camera poses for individual time steps, making our setup generalizable to moving hand-held cameras.

We then train dynamic NeRF [8] while refining the estimated time offsets and camera poses. We modify coarse-to-fine registration [21] to stabilize the training of the multiresolution grid-based representation. Furthermore, we propose a curriculum learning strategy that adds more variables as the optimization progresses. Optimization scheduling is critical for convergence in gradient-based optimization.

We evaluate our approach in the real-world CMU Panoptic Studio dataset [14] consisting of 9 seconds-long unsynchronized multi-view videos with a maximum of 4 seconds offsets without given camera poses. Experiments show that our initialization stage robustly aligns human motion, followed by a stable refinement stage that results in highly accurate calibration (rotation error $< 0.4^\circ$, translation error < 0.2 cm, time offset error < 0.03 frame in average).

2. Related Works

Human pose and shape estimation Since humans are one of the most common and important objects in the scene, there exist abundant datasets containing humans [1, 10, 13, 22, 25]. Recent methods leverage powerful data-driven prior to estimate human pose and shape from images or videos. Most approaches recover human pose and shape by estimating parametric models such as SMPL [24]. From optimization-based methods [3, 32], which leverage robust 2D joint estimation networks, to regression-based methods [15, 16, 18] that utilize 3D human datasets, early works faithfully recover 3D human pose and shape in camera coordinate. Recent advances [19, 37] take a step forward to estimate the global trajectories of humans, which is crucial for a complete understanding of human motion. Notably, SLAHMR [44] utilizes human motion priors to recover both real-world scaled global human motion and camera trajectory, whose scale is ambiguous with the SLAM pipeline alone. We note that monocular human shape and motion estimation works have matured and generalize well to novel scenes. In this paper, we explore the potential of human motion as a *robust mid-level representation* for calibration in both temporal and spatial domain.

Dynamic 3D scene reconstruction The emergence of NeRF [28] and its extension to the spatiotemporal domain enables immersive experience in a dynamic world, which was previously limited to a small navigatable area and requires a complicated capturing system [4]. One of the most common approaches to reconstruct 4D scenes is reconstructing 3D scenes in a canonical frame and optimize a deformation field to warp them [20, 23, 29, 30, 33, 43]. However, as pointed out by Park et al. [31], it is hard to let the deformation network learn general dynamics in practice. On the other hand, recent grid-based methods [5, 8] simply represent 4D scenes by introducing additional temporal domain without deformation field, which enables to represent general dynamic scenes easily. We exploit K-Planes [8] for our 4D scene representation due to its versatility.

However, all of the aforementioned dynamic NeRFs need synchronized videos and ground-truth camera poses. Recently, Sync-NeRF [17] aims to reconstruct dynamic NeRF from unsynchronized videos. They additionally optimize time offset parameters during the dynamic NeRF reconstruction process. However, Sync-NeRF requires initial time offsets close to ground truth since it can only deal with small temporal perturbations and they also require known camera poses.

Camera pose estimation with NeRF Since iNeRF [45] has shown that one can optimize camera poses given pre-trained NeRF with photometric loss, recent works attempt

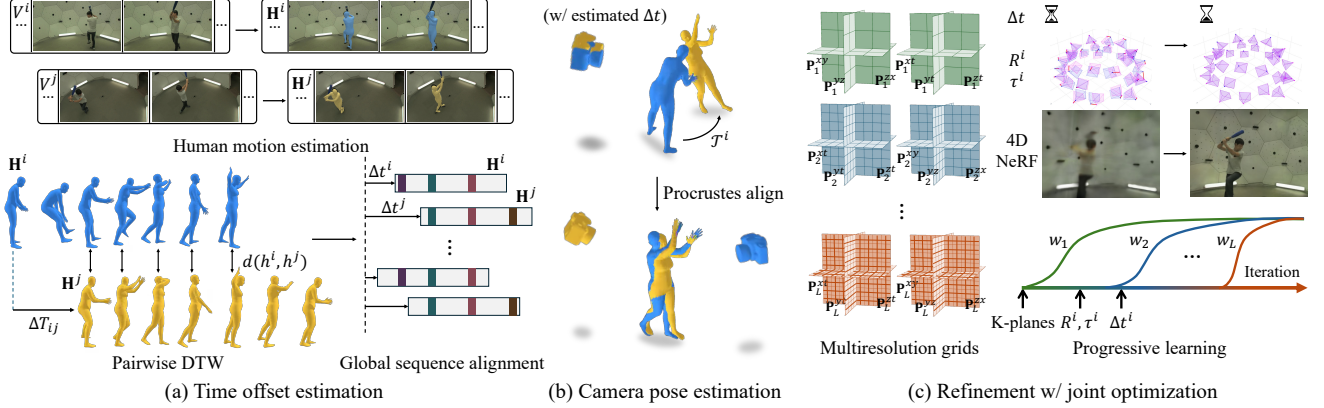


Figure 3. Overview of our method. Given unsynchronized multi-view videos without camera poses, we first extract human motion independently. Then we estimate (a) time offsets and (b) global camera poses by aligning human motions. Starting from the initial point, (c) we further refine both camera poses and time offsets by jointly optimizing them with dynamic NeRF with progressive training.

to reconstruct NeRF from unknown camera poses. They ease the burden of the hard requirements of NeRF (i.e., perfect camera poses) by jointly optimizing camera poses during the optimization process of NeRF. Instead of naïvely optimizing parameters [42], recent works show that coarse-to-fine optimization by progressively adding higher frequency bands [21] or curriculum learning strategy that progressively adds camera parameters [11]. However, previous works only optimize camera poses with *static* NeRF. To the best of our knowledge, we are the first to reconstruct dynamic NeRF from unknown time offsets and camera poses. We also observe that progressive training is critical for robust optimization in dynamic NeRF scenarios as well. We propose a similar coarse-to-fine optimization technique suited for multiresolution grid representation and curriculum learning strategy. More importantly, all previous works need *good initial points* and only adjust small misalignments during the optimization process or only work for image sets with extremely small baselines such as forward-facing captures [27]. We propose a novel way to obtain good initial points with humans, both for time offsets and camera poses.

3. Method

We reconstruct dynamic NeRF from unsynchronized multi-view videos with unknown camera poses. We first extract human motion of individual video in its own camera coordinate (Sec. 3.1). We then utilize extracted human motion as a calibration pattern to estimate both time offsets and camera poses of each videos (Sec. 3.2). Starting from the initial estimations, we further refine them by jointly optimizing calibration parameters meanwhile reconstructing dynamic NeRF (Sec. 3.3). Figure 3 describes the overall pipeline of our approach.

3.1. Problem Setup and Calibration Preparation

Problem setup We reconstruct dynamic NeRF from N unsynchronized multi-view videos $\{V^i\}_{i=1}^N$ whose poses are not known. Each video V^i contains M^i image frames, $V^i = (I_t^i; t \in [0, M^i - 1])$, where I_t^i is image of video frame at time t . We assume the dynamic scenes contain moving humans, but we do not assume that humans are the only dynamic objects. We estimate the time offset $\Delta t^i \in \mathbb{R}$ such that the timestamp t for the i th video V^i can be mapped to a synchronized global timestamp by adding time offset $t + \Delta t^i$. Furthermore, we aim to find camera poses in world coordinate, namely rotation R_t^i and translation τ_t^i of each videos.¹ Hereafter, we will use the term “calibration parameters” to refer to both time offsets and camera poses.

Human motion estimation We first estimate human motions in each multi-view video and use them as a cue to calibrate time offset and camera pose. We utilize SLAHMR [44] which is a method to recover 3D human motion from monocular video. Given a video V^i , we extract human motion \mathbf{H}^i which can be expressed as a time series,

$$\mathbf{H}^i = \left(\bigoplus_{k=1}^K h_{k,t}^i; t \in [0, M^i - 1] \right), \quad (1)$$

$$h_{k,t}^i = \{\Phi_{k,t}^i, \Theta_{k,t}^i, \beta_k^i, \Gamma_{k,t}^i\}, \quad (2)$$

where K is the number of humans in the scene, \bigoplus is concatenation operator, $h_{k,t}^i$ is state of the k th human at time t which is composed of root orientation $\Phi_{k,t}^i \in \mathbb{R}^3$, body pose $\Theta_{k,t}^i \in \mathbb{R}^{22 \times 3}$ that is modeled by relative 3D rotation of joints in axis-angle representation, position of root $\Gamma_{k,t}^i \in \mathbb{R}^3$, and human shape parameters $\beta_k^i \in \mathbb{R}^{16}$ which

¹We assume that camera intrinsics are known or already estimated with algorithms [12, 39].

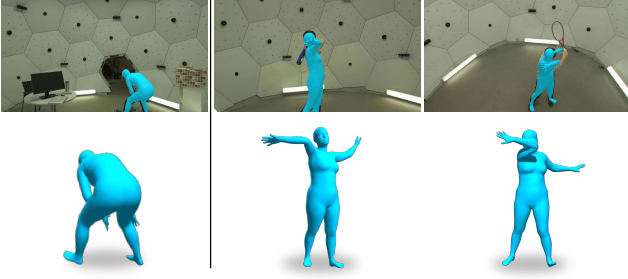


Figure 4. Examples of estimated human motion on our dataset. While SLAHMR [44] can reconstruct valid human motion for most frames (left), it sometimes fails when there is an ambiguity due to the viewing angle (middle) or fast motion (right).

remains constant across whole time. Human motions \mathbf{H}^i are extracted from each monocular video independently since videos are unsynchronized and we cannot leverage correspondence across different videos.

We can also obtain camera trajectory relative to human motion. First, we obtain camera trajectory with SLAM method [38] whose scale is ambiguous. Then, we recover scale with data-driven human motion priors during the optimization process following SLAHMR. For more details, we refer the readers to the original paper [44]. We demonstrate estimated human motion in Fig. 4. It is noteworthy that even the estimated human poses are not very accurate for some frames, we can robustly estimate calibration parameters with our initialization stage in Sec. 3.2.

3.2. Initialization Stage

With extracted human motions \mathbf{H} , we estimate time offsets of unsynchronized videos and camera poses in global coordinates. These estimated calibration parameters serve as initial points for refinement during the optimization of dynamic NeRF afterward (Sec. 3.3).

Time offset estimation We first estimate the time offset between a pair of videos, V^i and V^j . We consider time offset estimation as an alignment problem between time series of human motion \mathbf{H} . To do so, we define matching cost, or distance between arbitrary two states $h_{t_1}^i$ and $h_{t_2}^j$ from motion sequence \mathbf{H}^i and \mathbf{H}^j , respectively:

$$d(h_{t_1}^i, h_{t_2}^j) = \|\mathbf{J}_{\text{canon}, t_1}^i - \mathbf{J}_{\text{canon}, t_2}^j\|_2, \quad (3)$$

where $\mathbf{J}_{\text{canon}} \in \mathbb{R}^{22 \times 3}$ is a 3D positions of human body joints at canonical space. Joint positions can be obtained with SMPL-H [34] model \mathcal{S} , which takes root rotation, body pose, and shape parameter as input. We set root rotation as $\mathbf{0}$ to get joint positions at canonical frame,

$$\mathbf{J}_{\text{canon}, t}^i = \mathcal{S}_{\text{canon}}(h_t^i) = \mathcal{S}(\mathbf{0}, \Theta_t^i, \beta^i). \quad (4)$$

Algorithm 1: Global time offset alignment

Function GLOBAL ALIGN($C, \Delta T$):

Input : Cost matrix $C \in \mathbb{R}^{N \times N}$,
time offset matrix $\Delta T \in \mathbb{Z}^{N \times N}$

Output: Globally aligning time offsets $\Delta t \in \mathbb{Z}^N$

1 Globally aligning time offsets $\Delta t = \mathbf{0} \in \mathbb{Z}^N$

2 Globally aligned index group $\mathbf{G} = \emptyset$

3 Locally aligned index group list $\mathbf{G}_l = \emptyset$

4 Index list $\mathbf{I} = \{(i, j) | \forall i < j\}$

5 $\mathbf{I} \leftarrow \text{SORT}(\mathbf{I})$ \triangleright increasing order w.r.t. C_{ij}

6 $(i, j) \leftarrow \mathbf{I}[0]$ \triangleright anchor indices

7 $\Delta t[i] \leftarrow 0, \Delta t[j] \leftarrow \Delta T_{ij}$

8 Insert (i, j) to \mathbf{G}

9 **for** $k = \{1, \dots, N(N-1)/2 - 1\}$ **do**

10 $(i, j) \leftarrow \mathbf{I}[k]$

11 **if** $i \in \mathbf{G}, j \in \mathbf{G}$ **then**

12 | **continue**

13 **else if** $i \in \mathbf{G}, j \in \mathbf{G}_l[k], \exists k$ **then**

14 | Pop $\mathbf{G}_l[k]$ and add to \mathbf{G} after shift ΔT_{ij}

15 **else if** $i \in \mathbf{G}, j \notin \mathbf{G}, j \notin \mathbf{G}_l[k], \forall k$ **then**

16 | Add j to $\mathbf{G}, \Delta t[j] \leftarrow \Delta t[i] + \Delta T_{ij}$

17 **else if** $i \in \mathbf{G}_l[k], j \notin \mathbf{G}, j \notin \mathbf{G}_l[l], \forall l$ **then**

18 | Add j to $\mathbf{G}_l[k], \Delta t[j] \leftarrow \Delta t[i] + \Delta T_{ij}$

19 **else if** $i, j \notin \mathbf{G}, \notin \mathbf{G}_l[k], \forall k$ **then**

20 | Add (i, j) to new group in \mathbf{G}_l

21 | $\Delta t[i] \leftarrow 0, \Delta t[j] \leftarrow \Delta T_{ij}$

22 **else if** $i \in \mathbf{G}_l[k], j \in \mathbf{G}_l[l]$ **then**

23 | Pop $\mathbf{G}_l[l]$ and add to $\mathbf{G}_l[k]$ after shift ΔT_{ij}

24 **else if** $i, j \in \mathbf{G}_l[k]$ **then**

25 | **continue**

26 **else**

27 | vice versa for reverse case of (i, j)

28 **return** Δt

We use the explicit 3D joint positions for the loss instead of comparing distances directly from human pose parameter Θ_t and shape parameter β . The loss in the physical ambient space better reflects the actual deviation.

We exhaustively find all pairwise alignments of human motions and store them into two $N \times N$ matrices. Each pairwise alignment employs a dynamic time warping (DTW) algorithm, which is widely used in speech recognition [35].

$$C_{ij}, \Delta T_{ij} = \text{DTW}(\mathbf{H}^i, \mathbf{H}^j), \forall i < j, \quad (5)$$

where time offset matrix $\Delta T \in \mathbb{Z}^{N \times N}$ stores the estimated relative time offsets and cost matrix $C \in \mathbb{R}^{N \times N}$ stores the cost of the alignment at the estimated time offset. To calculate the cost with the DTW algorithm, we use the distance between human states defined in Eq. (3). We assume that every video V has the same frame rate, and we estimate time offset ΔT_{ij} as the most frequent warping time.

Then, we find the global sequence alignment of whole human motions with a greedy algorithm. First, we find an anchor index pair which has the minimum value $(i, j) = \text{argmin}_{(i, j)} C_{ij}$. Then, we incrementally add index pairs in increasing order with respect to the cost value.

$$\Delta t = \text{Global Align}(C, \Delta T), \quad (6)$$

where $\Delta t \in \mathbb{Z}^N$ is estimated time offsets that globally align human motions. A detailed pseudocode for the global alignment process is provided in Algorithm 1.

Camera pose estimation Next, we estimate camera poses by aligning human motions after the initial time offset estimation. Similar to the time offset estimation, we utilize 3D joint positions as calibration patterns. Different from time alignment, we extract joint positions by considering the orientation and translation of human roots:

$$\mathbf{J}_{\text{global},t}^i = \mathcal{S}_{\text{global}}(h_t^i) = \mathcal{S}(\Phi_t^i, \Theta_t^i, \beta^i) + \Gamma_t^i. \quad (7)$$

Then we find the optimal similarity transform $\mathcal{T}^i \in \text{SIM}(3)$ that minimizes the Procrustes distance between human motion \mathbf{H}^i and anchor human motion \mathbf{H}^α for all index i except the anchor index α ,

$$\mathcal{T}^i = \text{Procrustes} \left((\mathbf{J}_{\text{global},t+\Delta t^\alpha}^\alpha; t), (\mathbf{J}_{\text{global},t+\Delta t^i}^i; t) \right), \quad (8)$$

where anchor index α is randomly selected ($\alpha \in [1, N]$). We describe details of Procrustes analysis in the supplementary material.

Then we can obtain camera poses R_t^i, τ_t^i of the i th camera by applying the same similarity transform \mathcal{T}^i to camera poses that are obtained with human motions in Sec. 3.1.

3.3. Refinement with Dynamic NeRF Optimization

In this step, we further refine time offsets and camera poses, which are initialized properly in the initialization stage (Sec. 3.2) during the optimization of dynamic NeRF. We utilize K-Planes [8] as our dynamic NeRF representation. K-Planes uses six multi-resolution feature grids to represent 4D radiance fields. Namely, there are \mathbf{P}_l^{xy} , \mathbf{P}_l^{yz} , and \mathbf{P}_l^{zx} for space-only grids, \mathbf{P}_l^{xt} , \mathbf{P}_l^{yt} , and \mathbf{P}_l^{zt} for space-time grids, where $l \in [1, L]$ denotes the resolution level. For querying spatiotemporal point $\mathbf{q} = (\mathbf{x}, t)$, we can obtain the features by

$$f_l(\mathbf{q}) = \bigodot_c \psi(\mathbf{P}_l^c, \pi^c(\mathbf{q})), \quad (9)$$

where \bigodot is a Hadamard product, π^c is the projection operator that maps \mathbf{q} onto the c th plane, and ψ is a bilinear interpolation. Then, multi-level features are concatenated to a single feature vector $f(\mathbf{q})$

$$f(\mathbf{q}) = \bigoplus_{l=1}^L w_l f_l(\mathbf{q}), \quad (10)$$

where w_l is a weight multiplied to l -level feature vector. Volume density and color at spatiotemporal point \mathbf{q} with viewing direction \mathbf{d} can be obtained by

$$\sigma(\mathbf{q}), \hat{f}(\mathbf{q}) = \mathcal{F}_\sigma(f(\mathbf{q})), \quad (11)$$

$$\mathbf{c}(\mathbf{q}, \mathbf{d}) = \mathcal{F}_{\text{color}}(\hat{f}(\mathbf{q}), \gamma(\mathbf{d})), \quad (12)$$

where \mathcal{F}_σ and $\mathcal{F}_{\text{color}}$ are tiny MLP and γ is a positional embedder introduced in original NeRF [28]. Then, we can obtain pixel value at time t along a ray $\mathbf{r}_t^i = (\mathbf{o}_t^i, \mathbf{d}_t^i)$ with volume rendering formulation. \mathbf{o}_t^i and \mathbf{d}_t^i are camera center and ray direction which can be obtained with i th camera pose R_t^i, τ_t^i .

$$\hat{I} = \sum_{k=1}^N T_k (1 - e^{-\sigma(\mathbf{x}_k, t + \Delta t^i) \delta_k}) \mathbf{c}((\mathbf{x}_k, t + \Delta t^i), \mathbf{d}_t^i), \quad (13)$$

where $\mathbf{x}_k = \mathbf{o}_t^i + p_k \mathbf{d}_t^i$, $p_k \in [\text{near}, \text{far}]$ is the ray sample point on ray, $T_k = e^{-\sum_{j=1}^{k-1} \sigma_j \delta_j}$ is the accumulated transmittance, and δ is the distance between ray samples.

We optimize both 4D radiance fields and calibration parameters by minimizing photometric loss

$$\mathcal{L} = \sum_{i,t,\mathbf{r}} \|I_t^i(\mathbf{r}) - \hat{I}(\mathbf{r}_t^i, t + \Delta t^i)\|_2, \quad (14)$$

where $I_t^i(\mathbf{r})$ is a ground-truth pixel corresponding to randomly selected ray \mathbf{r} of t th frame of i th camera.

However, naively optimizing both dynamic NeRF and calibration parameters easily falls into bad local minima, although we have good initial points for camera poses and time offsets. We propose a progressive learning strategy for robust joint optimization of dynamic NeRF and calibration parameters.

First, we observe that coarse-to-fine registration is critical for dynamic NeRF. We weigh the feature from resolution level l by w_l before concatenated to single feature vector at Eq. (10):

$$w_l = \begin{cases} 0 & \text{if } \alpha < l - 1, \\ \frac{1 - \cos((\alpha - (l - 1))\pi)}{2} & \text{if } 0 \leq \alpha - (l - 1) < 1, \\ 1 & \text{if } \alpha - (l - 1) \geq 1 \end{cases}, \quad (15)$$

where $\alpha = L(e^\eta - 1)/(e - 1)$, $\eta \in [0, 1]$ is a normalized training step. This is in contrast to vanilla K-Planes [8] which uses all weights as 1. Our feature weighting strategy assigns big weights to low-frequency grids at the beginning of optimization stage and progressively increases weights of higher-resolution grids. Our strategy is inspired by the dynamic low-pass filter in BARF [21], but we instead modify the relative weights for grid resolution to effectively start from low-frequency features in multi-resolution K-Planes.

Furthermore, we propose a curriculum learning strategy for stable optimization. We first freeze camera poses and time offsets and only optimizes 4D NeRF for s_0 training steps. Then we add camera poses to the parameter list from s_0 iterations. Finally we add time offsets to learnable parameters and jointly optimize all parameters after another s_1 iterations. This progressive learning strategy is critical in preventing model from overfitting. This also aligns with observations from SCNeRF [11] that sequentially adds complexity to camera model.

4. Experiments

4.1. Experimental Setup

Dataset preparation We use CMU Panoptic Studio dataset [14] which contains dynamic sequences of human movement captured from 31 cameras surrounding the scene. Each of scenes contain various human motions, interactions with objects, and large portion of occlusions for some viewpoints. Note the view configuration is much harder than typical scenes such as NeRF blender scenes [28] that have 100 train views on upper hemisphere or LLFF dataset [27]. We take subsequences from sports and office sequence and make new dataset containing five scenes BASEBALL, TENNIS, OFFICE1, OFFICE2, and OFFICE3. Each multi-view training video is 270 frames long at 30 FPS and starts from a random global timestamp to make unsynchronized setup. All video sequences are sampled to have at least 150 overlapping frames. Namely, maximum time offset between two videos is 120 frames. The ground truth time offsets and camera poses are used for evaluation, and not provided to the system. We use 29 or 30 cameras for training dynamic NeRF, and one camera for test novel-view synthesis performance.

Implementation details We undistort all training images before estimating human motion and training dynamic NeRFs with provided radial and tangential distortion parameters. We optimize K-Planes with Adam optimizer [7] with rendering loss in Eq. (14) and regularization losses including total variance in space, time smoothness loss, density L1 loss, and sparse transient loss introduced in original K-Planes [8]. We also use proposal sampling [2] to sample ray points for volume rendering. Although we first estimate camera poses for all timestamps in the initialization stage, we only use the camera poses at the first timestamp for simplicity since our dataset contains only static multi-view cameras. We further optimize one camera pose for each video at refinement. We jointly optimize calibration parameters and K-Planes for total 300k iterations and finish coarse-to-fine scheduling at 100k iterations. We use grid resolution of 240 for time axis, multi-scale level of $L = 4$ or 5 depending on scenes, at the maximum resolution of 384. We unfreeze camera pose parameters at $s_0 = 2k$ steps, time offset parameters at $s_0 + s_1 = 20k$ steps.

4.2. Alignment Performance

First, we report the accuracy of time synchronization and camera pose estimation in Tab. 1. We measure errors after aligning estimated results to ground truth to recover original scale, orientation, and shifts. Both quantitative results in Tab. 1 (“Init” column) and visual illustration Fig. 5 (left) show that our initialization step can achieve reasonable first estimation. Our first alignment with human motion achieves

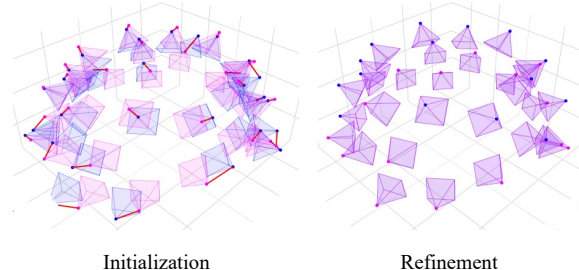


Figure 5. We visualize estimated camera poses of the initialization step (left) and the refinement step (right) on OFFICE2 scene. Blue and red frustums are estimation and ground truth, respectively.

Scene	Rotation (°)		Trans. (cm)		Δt (frames)		
	Init	Refine	Init	Refine	Data	Init	Refine
BASEBALL	5.302	0.328	22.582	0.158	58.10	0.700	0.025
OFFICE1	3.883	0.420	19.754	0.171	68.35	3.448	0.031
OFFICE2	8.889	0.660	37.971	0.372	56.42	1.300	0.029
OFFICE3	3.946	0.363	19.242	0.165	60.03	0.800	0.026
TENNIS	5.293	0.290	25.827	0.217	69.06	0.467	0.028
Average	5.463	0.412	25.075	0.217	62.39	1.343	0.028

Table 1. Quantitative results on camera pose estimation and time synchronization. We report the results from the first initialization stage (Init) and the second refinement stage (Refine).

camera pose calibration with a rotation error of less than 5.5° and a translation error of less than 26 cm on average, despite the absence of any input camera pose information. Furthermore, our initialization strategy can estimate fairly accurate time offsets (average 1.34 frames) even from severely unsynchronized videos (62.39 frames time offset on average). Starting from the initial estimation, our refinement with joint optimization of 4D NeRF can achieve near-perfect calibration as shown in Tab. 1 (“Refine” column) and Fig. 5 (right). Our approach aligns camera poses within rotation error of 0.4° and translation error of 0.22 cm on average. Also the error of estimated time offsets is less than 0.03 frames on average, which is equal to 1 millisecond.

We also test to use different distance function, or matching cost between two human states. Instead of L2 distance between 3D joint positions as defined in Eq. (3), we test naïve L2 distance between human shape and pose parameters for time offset estimation at initialization step:

$$d(h_{t_1}^i, h_{t_2}^j) = \|\Theta_{t_1}^i, \beta^i - \Theta_{t_2}^j, \beta^j\|_2. \quad (16)$$

As shown in Tab. 2 (first row), replacing the distance function degrades the time synchronization performance significantly considering we are using the same SMPL sequence.

We further investigate the robustness of our initialization stage. First, we measure time offset and camera pose estimation error after applying synthetic image degradation and color variations to each training video V^i . We apply gamma correction with randomly sampled within uniform

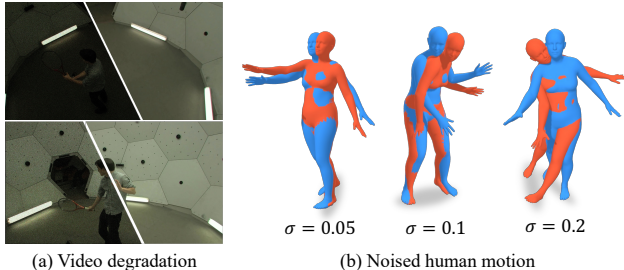


Figure 6. Visual examples of (a) video degradation and (b) perturbed human motion with Gaussian noise of various σ to test robustness of our method. Blue human meshes are initially estimated human motion and red meshes are noised results.

TENNIS scene	Rotation ($^{\circ}$)		Trans. (cm)		Δt (frames)	
	Init	Refine	Init	Refine	Init	Refine
L2 norm, β , Θ	5.382	0.656	26.130	0.261	2.100	0.030
SMPL noise, $\sigma = 0.01$	5.266	0.285	25.844	0.296	1.633	0.027
SMPL noise, $\sigma = 0.02$	5.307	1.240	25.825	0.276	0.533	0.028
SMPL noise, $\sigma = 0.05$	5.310	0.357	25.861	0.277	0.833	0.029
SMPL noise, $\sigma = 0.1$	5.241	0.518	25.383	0.257	2.100	0.030
SMPL noise, $\sigma = 0.2$	5.404	0.934	26.831	0.217	2.367	0.024
Degraded video	6.496	-	32.374	-	1.133	-
Default setup	5.293	0.290	25.827	0.217	0.467	0.028

Table 2. Quantitative results with input degradation², noised human motion, and different choice of human state distance.

range $\gamma \sim [0.35, 2.1]$ for color variations and we add luminance noise and chromatic noise for image degradation. We also add noise to human shape parameter β^i and pose parameter Θ_t^i to test robustness on accuracy of SMPL parameter estimation. Samples of degraded images and noised human motion can be found in Fig. 6.

We report quantitative results on robustness experiments in Tab. 2. Although the alignment performance with degraded videos is degraded compared to the original setup, still our approach produces reasonable time offsets and camera poses for initialization considering the severe appearance variation and quality degradation. This result supports our claim that human motion can serve as a robust mid-level representation for calibration. Our approach also shows comparable accuracy to the original data when the noise level is moderate ($\sigma \leq 0.05$). This results show that our aligning strategy is not sensitive to the quality of extracted human motion. Although time offset errors increase at severe noise level ($\sigma \geq 0.1$), our approach reduces the temporal misalignment drastically (from 69.06 of input data to less than 2.5). Furthermore, calibration parameters initialized from noised human motions were sufficiently accurate to recover precise time offsets and camera poses in the subsequent refinement step, as shown in Tab. 2.

²We do not test refinement for the degraded video setup since NeRFs cannot fit scenes that have severe appearance inconsistency across videos.

4.3. Dynamic Novel-view Synthesis

To evaluate our dynamic scene reconstruction performance, we measure novel view synthesis errors. We measure photometric error for rendered images at test view only for timestamps that are overlapped by all of training videos since we take unsynchronized videos as input. We also conduct test-time optimization for accurate measurement that freezes NeRF parameters and optimizes only test camera poses and timestamps for small iterations before measure metrics. Since we are the first approach to reconstruct dynamic NeRF without any assumption of both camera poses and time synchronization, there is no existing work to compare with our method that has exactly same problem setup. Instead, we compare our approach to Sync-NeRF [17] which is a method that jointly optimizes time offsets with dynamic NeRF. Since Sync-NeRF cannot align camera poses, we relax our problem setup for Sync-NeRF by providing ground-truth camera poses. We also compare our method with the oracle, namely, K-Planes with ground-truth camera poses and time offsets provided by dataset.

Quantitative results of novel view synthesis in mean PSNR, SSIM [41], LPIPS [46] are reported in Tab. 3. Our approach achieves superior performance across all metrics compared to Sync-NeRF even if Sync-NeRF baseline uses ground-truth camera poses. It supports our claim that good initial point (time offset for Sync-NeRF comparison) is critical for gradient-based optimization. Without proper initialization of time offsets, Sync-NeRF cannot reconstruct high-quality dynamic scenes. Furthermore, our approach achieves almost on par performance to the oracle model. We observe that our approach achieves a slightly higher PSNR than the oracle in the BASEBALL scene. This is possible because the ground-truth camera poses in the real-world dataset are not perfectly accurate, and our method optimizes time offsets to subframe precision. We show qualitative results which are rendered at novel viewpoints in Fig. 7. Our approach achieves superior rendering quality compared to Sync-NeRF baseline and comparable results compared to the oracle model, which is aligned with the quantitative results. Sync-NeRF cannot calibrate time offsets without proper initialization and cannot reconstruct dynamic objects consequently. Videos rendered at novel viewpoints can be found in the supplementary material.

Additionally, we test our approach without our progressive learning strategy with initialized calibration parameters. Quantitative results and qualitative results are also included in Tab. 3 and Fig. 7, respectively. Even starting with proper camera poses and time offsets estimated by our initialization stage, without progressive training, the reconstructed dynamic scenes show inferior quality. This result validates the importance of the proposed progressive learning strategy.



Figure 7. Qualitative comparison of novel view synthesis performance.

Scene	Sync-NeRF w/ GT pose			Ours w/o prog. training			Ours			Oracle (GT pose & time)		
	PSNR	SSIM	LPIPS	PSNR	SSIM	LPIPS	PSNR	SSIM	LPIPS	PSNR	SSIM	LPIPS
BASEBALL	21.17	0.833	0.189	19.23	0.577	0.412	27.20	0.919	0.072	26.80	0.925	0.065
OFFICE1	20.62	0.809	0.196	22.33	0.678	0.334	26.65	0.855	0.125	27.00	0.905	0.079
OFFICE2	21.14	0.782	0.195	18.39	0.511	0.544	24.43	0.820	0.155	26.58	0.891	0.091
OFFICE3	20.94	0.826	0.178	21.06	0.614	0.383	27.51	0.893	0.093	28.23	0.912	0.077
TENNIS	22.09	0.851	0.168	17.29	0.531	0.552	26.94	0.881	0.113	27.22	0.916	0.080
Average	21.19	0.820	0.185	19.66	0.582	0.445	26.55	0.874	0.112	27.16	0.910	0.078

Table 3. Quantitative comparison of novel view synthesis performance.

5. Conclusion

We propose a practical solution to reconstruct neural dynamic 3D scenes containing humans from unsynchronized and uncalibrated multi-view videos. Given human motion of individual videos, we find the initial estimates of temporal offsets and camera poses, which are highly robust to occlusions or other adversaries. We then train 4D NeRF volume in a coarse-to-fine fashion which effectively stabilize the optimization process. During training, we progressively add the estimated parameters into a joint optimization routine and further refine them. We demonstrate that we can acquire reliable dynamic scene reconstruction in challenging setups performing on par with accurate calibration.

Limitations & future works Although our initialization stage robustly estimates time offsets and camera poses for

most cases thanks to the temporal aggregation, we cannot recover calibration parameters if SLAHMR [44] completely fails to recover human motion from video. Nevertheless, we anticipate that as advancements in human motion estimation continue, our approach will benefit from these improvements. Our formulation is general enough to be applicable even when all cameras are in motion; however, we have not yet empirically validated this scenario, and increased degrees of freedom may require additional optimization techniques. Additionally, integrating techniques that address varying appearance and occlusions (e.g., appearance embedding and uncertainty estimation [26]) could enable our method to reconstruct complex scenes from distributed videos, such as concert halls or sports games, directly from fan-captured internet videos.

References

- [1] Mykhaylo Andriluka, Leonid Pishchulin, Peter Gehler, and Bernt Schiele. 2d human pose estimation: New benchmark and state of the art analysis. In *Proceedings of the IEEE Conference on Computer Vision and Pattern Recognition (CVPR)*, 2014. 2
- [2] Jonathan T Barron, Ben Mildenhall, Dor Verbin, Pratul P Srinivasan, and Peter Hedman. Mip-nerf 360: Unbounded anti-aliased neural radiance fields. In *Proceedings of the IEEE/CVF conference on computer vision and pattern recognition*, pages 5470–5479, 2022. 6
- [3] Federica Bogo, Angjoo Kanazawa, Christoph Lassner, Peter Gehler, Javier Romero, and Michael J Black. Keep it smpl: Automatic estimation of 3d human pose and shape from a single image. In *Computer Vision—ECCV 2016: 14th European Conference, Amsterdam, The Netherlands, October 11–14, 2016, Proceedings, Part V 14*, pages 561–578. Springer, 2016. 2
- [4] Michael Broxton, John Flynn, Ryan Overbeck, Daniel Erickson, Peter Hedman, Matthew Duvall, Jason Dourgarian, Jay Busch, Matt Whalen, and Paul Debevec. Immersive light field video with a layered mesh representation. *ACM Transactions on Graphics (TOG)*, 39(4):86–1, 2020. 2
- [5] Ang Cao and Justin Johnson. Hexplane: A fast representation for dynamic scenes. In *Proceedings of the IEEE/CVF Conference on Computer Vision and Pattern Recognition (CVPR)*, pages 130–141, 2023. 1, 2
- [6] Yudi Dai, Yitai Lin, Xiping Lin, Chenglu Wen, Lan Xu, Hongwei Yi, Siqi Shen, Yuexin Ma, and Cheng Wang. Sloper4d: A scene-aware dataset for global 4d human pose estimation in urban environments. In *Proceedings of the IEEE/CVF Conference on Computer Vision and Pattern Recognition (CVPR)*, pages 682–692, 2023. 1
- [7] P Kingma Diederik. Adam: A method for stochastic optimization. (*No Title*), 2014. 6
- [8] Sara Fridovich-Keil, Giacomo Meanti, Frederik Rahbæk Warburg, Benjamin Recht, and Angjoo Kanazawa. K-planes: Explicit radiance fields in space, time, and appearance. In *Proceedings of the IEEE/CVF Conference on Computer Vision and Pattern Recognition (CVPR)*, pages 12479–12488, 2023. 1, 2, 5, 6
- [9] Hang Gao, Ruilong Li, Shubham Tulsiani, Bryan Russell, and Angjoo Kanazawa. Monocular dynamic view synthesis: A reality check. *Advances in Neural Information Processing Systems*, 35:33768–33780, 2022. 1
- [10] Catalin Ionescu, Dragos Papava, Vlad Olaru, and Cristian Sminchisescu. Human3.6m: Large scale datasets and predictive methods for 3d human sensing in natural environments. *IEEE transactions on pattern analysis and machine intelligence*, 36(7):1325–1339, 2013. 1, 2
- [11] Yoonwoo Jeong, Seokjun Ahn, Christopher Choy, Anima Anandkumar, Minsu Cho, and Jaesik Park. Self-calibrating neural radiance fields. In *Proceedings of the IEEE/CVF International Conference on Computer Vision*, pages 5846–5854, 2021. 3, 5
- [12] Linyi Jin, Jianming Zhang, Yannick Hold-Geoffroy, Oliver Wang, Kevin Blackburn-Matzen, Matthew Sticha, and David F. Fouhey. Perspective fields for single image camera calibration. In *Proceedings of the IEEE/CVF Conference on Computer Vision and Pattern Recognition (CVPR)*, pages 17307–17316, 2023. 3
- [13] Sam Johnson and Mark Everingham. Clustered pose and nonlinear appearance models for human pose estimation. In *bmvc*, page 5. Aberystwyth, UK, 2010. 2
- [14] Hanbyul Joo, Tomas Simon, Xulong Li, Hao Liu, Lei Tan, Lin Gui, Sean Banerjee, Timothy Scott Godisart, Bart Nabbe, Iain Matthews, Takeo Kanade, Shohei Nobuhara, and Yaser Sheikh. Panoptic studio: A massively multiview system for social interaction capture. *IEEE Transactions on Pattern Analysis and Machine Intelligence*, 2017. 1, 2, 6
- [15] Angjoo Kanazawa, Michael J Black, David W Jacobs, and Jitendra Malik. End-to-end recovery of human shape and pose. In *Proceedings of the IEEE conference on computer vision and pattern recognition*, pages 7122–7131, 2018. 2
- [16] Angjoo Kanazawa, Jason Y Zhang, Panna Felsen, and Jitendra Malik. Learning 3d human dynamics from video. In *Proceedings of the IEEE/CVF conference on computer vision and pattern recognition*, pages 5614–5623, 2019. 2
- [17] Seoha Kim, Jeongmin Bae, Youngsik Yun, Hahyun Lee, Gun Bang, and Youngjung Uh. Sync-nerf: Generalizing dynamic nerfs to unsynchronized videos. In *Proceedings of the AAAI Conference on Artificial Intelligence*, pages 2777–2785, 2024. 2, 7
- [18] Muhammed Kocabas, Nikos Athanasiou, and Michael J. Black. Vibe: Video inference for human body pose and shape estimation. In *Proceedings of the IEEE/CVF Conference on Computer Vision and Pattern Recognition (CVPR)*, 2020. 2
- [19] Muhammed Kocabas, Ye Yuan, Pavlo Molchanov, Yunrong Guo, Michael J Black, Otmar Hilliges, Jan Kautz, and Umar Iqbal. Pace: Human and camera motion estimation from in-the-wild videos. In *2024 International Conference on 3D Vision (3DV)*, pages 397–408. IEEE, 2024. 2
- [20] Zhengqi Li, Simon Niklaus, Noah Snavely, and Oliver Wang. Neural scene flow fields for space-time view synthesis of dynamic scenes. In *Proceedings of the IEEE/CVF Conference on Computer Vision and Pattern Recognition*, pages 6498–6508, 2021. 2
- [21] Chen-Hsuan Lin, Wei-Chiu Ma, Antonio Torralba, and Simon Lucey. Barf: Bundle-adjusting neural radiance fields. In *Proceedings of the IEEE/CVF international conference on computer vision*, pages 5741–5751, 2021. 2, 3, 5
- [22] Tsung-Yi Lin, Michael Maire, Serge Belongie, James Hays, Pietro Perona, Deva Ramanan, Piotr Dollár, and C Lawrence Zitnick. Microsoft coco: Common objects in context. In *Computer Vision—ECCV 2014: 13th European Conference, Zurich, Switzerland, September 6–12, 2014, Proceedings, Part V 13*, pages 740–755. Springer, 2014. 2
- [23] Yu-Lun Liu, Chen Gao, Andreas Meuleman, Hung-Yu Tseng, Ayush Saraf, Changil Kim, Yung-Yu Chuang, Johannes Kopf, and Jia-Bin Huang. Robust dynamic radiance fields. In *Proceedings of the IEEE/CVF Conference on Computer Vision and Pattern Recognition*, pages 13–23, 2023. 2
- [24] Matthew Loper, Naureen Mahmood, Javier Romero, Gerard

- Pons-Moll, and Michael J. Black. Smpl: a skinned multi-person linear model. *ACM Trans. Graph.*, 34(6), 2015. 2
- [25] Naureen Mahmood, Nima Ghorbani, Nikolaus F. Troje, Gerard Pons-Moll, and Michael J. Black. Amass: Archive of motion capture as surface shapes. In *Proceedings of the IEEE/CVF International Conference on Computer Vision (ICCV)*, 2019. 2
- [26] Ricardo Martin-Brualla, Noha Radwan, Mehdi SM Sajjadi, Jonathan T Barron, Alexey Dosovitskiy, and Daniel Duckworth. Nerf in the wild: Neural radiance fields for unconstrained photo collections. In *Proceedings of the IEEE/CVF conference on computer vision and pattern recognition*, pages 7210–7219, 2021. 8
- [27] Ben Mildenhall, Pratul P. Srinivasan, Rodrigo Ortiz-Cayon, Nima Khademi Kalantari, Ravi Ramamoorthi, Ren Ng, and Abhishek Kar. Local light field fusion: practical view synthesis with prescriptive sampling guidelines. *ACM Trans. Graph.*, 38(4), 2019. 3, 6
- [28] Ben Mildenhall, Pratul P Srinivasan, Matthew Tancik, Jonathan T Barron, Ravi Ramamoorthi, and Ren Ng. Nerf: Representing scenes as neural radiance fields for view synthesis. *Communications of the ACM*, 65(1):99–106, 2021. 2, 5, 6
- [29] Keunhong Park, Utkarsh Sinha, Jonathan T Barron, Sofien Bouaziz, Dan B Goldman, Steven M Seitz, and Ricardo Martin-Brualla. Nerfies: Deformable neural radiance fields. In *Proceedings of the IEEE/CVF International Conference on Computer Vision*, pages 5865–5874, 2021. 2
- [30] Keunhong Park, Utkarsh Sinha, Peter Hedman, Jonathan T. Barron, Sofien Bouaziz, Dan B Goldman, Ricardo Martin-Brualla, and Steven M. Seitz. Hypernerf: a higher-dimensional representation for topologically varying neural radiance fields. *ACM Trans. Graph.*, 40(6), 2021. 1, 2
- [31] Sungheon Park, Minjung Son, Seokhwan Jang, Young Chun Ahn, Ji-Yeon Kim, and Nahyup Kang. Temporal interpolation is all you need for dynamic neural radiance fields. In *Proceedings of the IEEE/CVF Conference on Computer Vision and Pattern Recognition*, pages 4212–4221, 2023. 2
- [32] Georgios Pavlakos, Vasileios Choutas, Nima Ghorbani, Timo Bolkart, Ahmed A. A. Osman, Dimitrios Tzionas, and Michael J. Black. Expressive body capture: 3d hands, face, and body from a single image. In *Proceedings of the IEEE/CVF Conference on Computer Vision and Pattern Recognition (CVPR)*, 2019. 2
- [33] Albert Pumarola, Enric Corona, Gerard Pons-Moll, and Francesc Moreno-Noguer. D-nerf: Neural radiance fields for dynamic scenes. In *Proceedings of the IEEE/CVF Conference on Computer Vision and Pattern Recognition*, pages 10318–10327, 2021. 2
- [34] Javier Romero, Dimitrios Tzionas, and Michael J. Black. Embodied hands: modeling and capturing hands and bodies together. *ACM Trans. Graph.*, 36(6), 2017. 4
- [35] Hiroaki Sakoe and Seibi Chiba. Dynamic programming algorithm optimization for spoken word recognition. *IEEE transactions on acoustics, speech, and signal processing*, 26(1):43–49, 1978. 4
- [36] Johannes Lutz Schönberger and Jan-Michael Frahm. Structure-from-motion revisited. In *Conference on Computer Vision and Pattern Recognition (CVPR)*, 2016. 2
- [37] Yu Sun, Qian Bao, Wu Liu, Tao Mei, and Michael J Black. Trace: 5d temporal regression of avatars with dynamic cameras in 3d environments. In *Proceedings of the IEEE/CVF Conference on Computer Vision and Pattern Recognition*, pages 8856–8866, 2023. 2
- [38] Zachary Teed and Jia Deng. Droid-slam: Deep visual slam for monocular, stereo, and rgb-d cameras. *Advances in neural information processing systems*, 34:16558–16569, 2021. 4
- [39] Alexander Veicht, Paul-Edouard Sarlin, Philipp Lindenberger, and Marc Pollefeys. GeoCalib: Single-image Calibration with Geometric Optimization. In *ECCV*, 2024. 3
- [40] Shuzhe Wang, Vincent Leroy, Yohann Cabon, Boris Chidlovskii, and Jerome Revaud. Dust3r: Geometric 3d vision made easy. In *CVPR*, 2024. 2
- [41] Zhou Wang, Alan C Bovik, Hamid R Sheikh, and Eero P Simoncelli. Image quality assessment: from error visibility to structural similarity. *IEEE transactions on image processing*, 13(4):600–612, 2004. 7
- [42] Zirui Wang, Shangzhe Wu, Weidi Xie, Min Chen, and Victor Adrian Prisacariu. Nerf-: Neural radiance fields without known camera parameters. *arXiv preprint arXiv:2102.07064*, 2021. 3
- [43] Gengshan Yang, Minh Vo, Natalia Neverova, Deva Ramanan, Andrea Vedaldi, and Hanbyul Joo. Banmo: Building animatable 3d neural models from many casual videos. In *Proceedings of the IEEE/CVF Conference on Computer Vision and Pattern Recognition (CVPR)*, pages 2863–2873, 2022. 2
- [44] Vickie Ye, Georgios Pavlakos, Jitendra Malik, and Angjoo Kanazawa. Decoupling human and camera motion from videos in the wild. In *Proceedings of the IEEE/CVF conference on computer vision and pattern recognition*, pages 21222–21232, 2023. 2, 3, 4, 8
- [45] Lin Yen-Chen, Pete Florence, Jonathan T Barron, Alberto Rodriguez, Phillip Isola, and Tsung-Yi Lin. inerf: Inverting neural radiance fields for pose estimation. In *2021 IEEE/RSJ International Conference on Intelligent Robots and Systems (IROS)*, pages 1323–1330. IEEE, 2021. 2
- [46] Richard Zhang, Phillip Isola, Alexei A Efros, Eli Shechtman, and Oliver Wang. The unreasonable effectiveness of deep features as a perceptual metric. In *Proceedings of the IEEE conference on computer vision and pattern recognition*, pages 586–595, 2018. 7

Humans as a Calibration Pattern: Dynamic 3D Scene Reconstruction from Unsynchronized and Uncalibrated Videos

Supplementary Material

A. Implementation Details

In this section, we describe details that we could not address in the main manuscript. We describe additional details to train K-Planes, which is our dynamic NeRF representation in Appendix A.1, Procrustes alignment used in camera pose estimation in Appendix A.2, and details regarding evaluation in Appendix A.3.

A.1. Training K-Planes

We use $L = 5$ spatial grid resolutions [24, 48, 96, 192, 384] for OFFICE1, OFFICE2, OFFICE3, and TENNIS scenes, and we use $L = 4$ grid resolutions [48, 96, 192, 384] for BASEBALL scene. We observe that BASEBALL scene converges well starting from the resolution of 48. We use a single resolution, 240, for the temporal grid in all scenes.

In addition to the weight scheduling described in the main manuscript, we also schedule the weights of regularization terms. We apply cosine scheduling that decreases weights to 1/100 of its initial weights at the end of the scheduling. We use weights 0.01 for distortion loss, 0.001 for L1 loss in time planes, 0.001 for total variance loss in spatial planes, 0.01 for time smoothness loss, and 0.01 for density L1 loss. We start scheduling of regularization from 100k steps for OFFICE1, OFFICE2, OFFICE3, and TENNIS scenes and 50k steps for BASEBALL scene, and end scheduling at 150k steps.

For efficiency, we initialize feature values of finer grids by bilinear interpolation of values from coarser grids. Namely, we initialize finer grids \mathbf{P}_l^c , ($l > 1$) at $\alpha = l - 1$ with values interpolated from \mathbf{P}_{l-1}^c , where $\alpha = L(e^\eta - 1)/(e - 1)$, $\eta \in [0, 1]$ is a normalized training step.

A.2. Procrustes Alignment

As we describe in Eq. (8) in the main manuscript, we estimate similarity transform between two 3D joint positions. We first estimate scale, translation, and rotation that align target joint positions ($\mathbf{J}_{\text{global}, t+\Delta t^i}^i; t$) to the reference joint positions of anchor index α , ($\mathbf{J}_{\text{global}, t+\Delta t^\alpha}^\alpha; t$) with Procrustes analysis,

$$s_i, s_\alpha, \mathbf{t}_i, \mathbf{t}_\alpha, R = \text{PROCRUSTES}((\mathbf{J}_{\text{global}, t+\Delta t^i}^i; t), (\mathbf{J}_{\text{global}, t+\Delta t^\alpha}^\alpha; t)). \quad (17)$$

We describe details of the Procrustes analysis in Algorithm 2. Then we can obtain camera poses in the global coordinate (i.e., camera coordinate of anchor index) by applying estimated transformation to the camera poses in the

Algorithm 2: Procrustes analysis

Function PROCRUSTES(X, Y):

Input : Point set to align $X = \{\mathbf{x}_i | \mathbf{x}_i \in \mathbb{R}^3\}_{i=1}^N$,
Reference point set $Y = \{\mathbf{y}_i | \mathbf{y}_i \in \mathbb{R}^3\}_{i=1}^N$
Output: scale s_x, s_y , translation $\mathbf{t}_x, \mathbf{t}_y$, rotation R

```

1   $\mathbf{t}_x \leftarrow \sum \mathbf{x}_i / N, \mathbf{t}_y \leftarrow \sum \mathbf{y}_i / N$ 
2   $s_x \leftarrow \sqrt{\sum \|\mathbf{x}_i - \mathbf{t}_x\|_2^2 / N}$ 
3   $s_y \leftarrow \sqrt{\sum \|\mathbf{y}_i - \mathbf{t}_y\|_2^2 / N}$ 
4   $\hat{X} \leftarrow \frac{1}{s_x}([\mathbf{x}_i] - \mathbf{t}_x)$ 
5   $\hat{Y} \leftarrow \frac{1}{s_y}([\mathbf{y}_i] - \mathbf{t}_y)$ 
6   $U, \Sigma, V^* \leftarrow \text{SVD}(\hat{Y} \hat{X}^\top)$ 
7   $R \leftarrow UV^{*\top}$ 
8  return  $s_x, s_y, \mathbf{t}_x, \mathbf{t}_y, R$ 

```

Algorithm 3: Align cameras

Function ALIGN CAM($\{R_{\text{est}}^i, \tau_{\text{est}}^i\}, \{R_{\text{ref}}^i, \tau_{\text{ref}}^i\}$):

Input : Estimated camera poses $\{R_{\text{est}}^i, \tau_{\text{est}}^i\}$,
Reference camera poses $\{R_{\text{ref}}^i, \tau_{\text{ref}}^i\}$

Output: Aligned estimated camera poses $\{\tilde{R}_{\text{est}}^i, \tilde{\tau}_{\text{est}}^i\}$

```

1  Estimated camera centers  $\mathbf{o}_{\text{est}}^i \leftarrow -R_{\text{est}}^{i\top} \tau_{\text{est}}^i$ 
2  Reference camera centers  $\mathbf{o}_{\text{ref}}^i \leftarrow -R_{\text{ref}}^{i\top} \tau_{\text{ref}}^i$ 
3   $s_{\text{est}}, s_{\text{ref}}, \mathbf{t}_{\text{est}}, \mathbf{t}_{\text{ref}}, R \leftarrow \text{PROCRUSTES}(\{\mathbf{o}_{\text{est}}^i\}, \{\mathbf{o}_{\text{ref}}^i\})$ 
4   $\tilde{\mathbf{o}}_{\text{est}}^i \leftarrow s_{\text{ref}} R (\frac{1}{s_{\text{est}}}(\mathbf{o}_{\text{est}}^i - \mathbf{t}_{\text{est}})) + \mathbf{t}_{\text{ref}}$ 
5   $\tilde{R}_{\text{est}}^i \leftarrow R_{\text{est}}^i R^\top$ 
6   $\tilde{\tau}_{\text{est}}^i \leftarrow -\tilde{R}_{\text{est}}^{i\top} \tilde{\mathbf{o}}_{\text{est}}^i$ 
7  return  $\{\tilde{R}_{\text{est}}^i, \tilde{\tau}_{\text{est}}^i\}$ 

```

i th camera's coordinate, R^i, τ^i similar to line 3-7 in Algorithm 3.

A.3. Evaluation Details

In this section, we provide additional details for evaluation of our method. Since we only optimize camera poses and time offsets of training videos, we do not have accurate poses and time offsets of test videos in the coordinate system that we are optimizing training camera poses and time offsets. Therefore, we first transform ground-truth test camera poses by aligning the ground-truth training camera poses to the estimated training camera poses. Starting from the transformed test camera poses, we further optimize camera poses while freezing NeRF parameters with supervision of test view video frames before measuring errors of rendered images.

Since the estimated camera poses are up to 3D similarity transformation (scale, rotation, and translation), we align our estimated camera poses to the ground-truth training camera poses before measuring pose errors. Detailed description of camera alignment procedures used in both novel-view synthesis performance measurement and camera pose accuracy can be found in Algorithm 3.

B. Additional Results

We visualize both initialized and refined camera poses at the top row and bottom row, respectively, in all of the scenes in our dataset in Fig. 8. We can observe that our initialization step produces good initial points, and our joint optimization with dynamic NeRF produces near-perfect pose alignments across all scenes.

Furthermore, we show additional qualitative comparisons in Fig. 9. We also provide videos rendered at the test viewpoint in the supplementary material. We recommend the readers to see the videos.

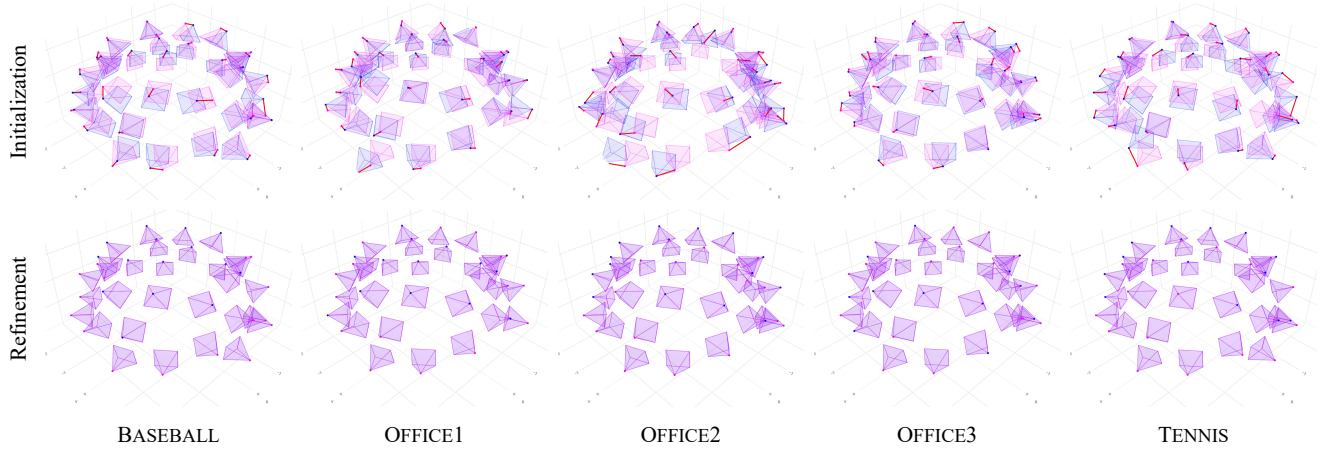


Figure 8. We demonstrate camera pose estimation results of the initialization stage at the top row (Initialization) and the final results of the joint optimization with K-Planes at the bottom row (Refinement). Red frustums are the ground-truth camera poses and blue frustums are the estimated camera poses.

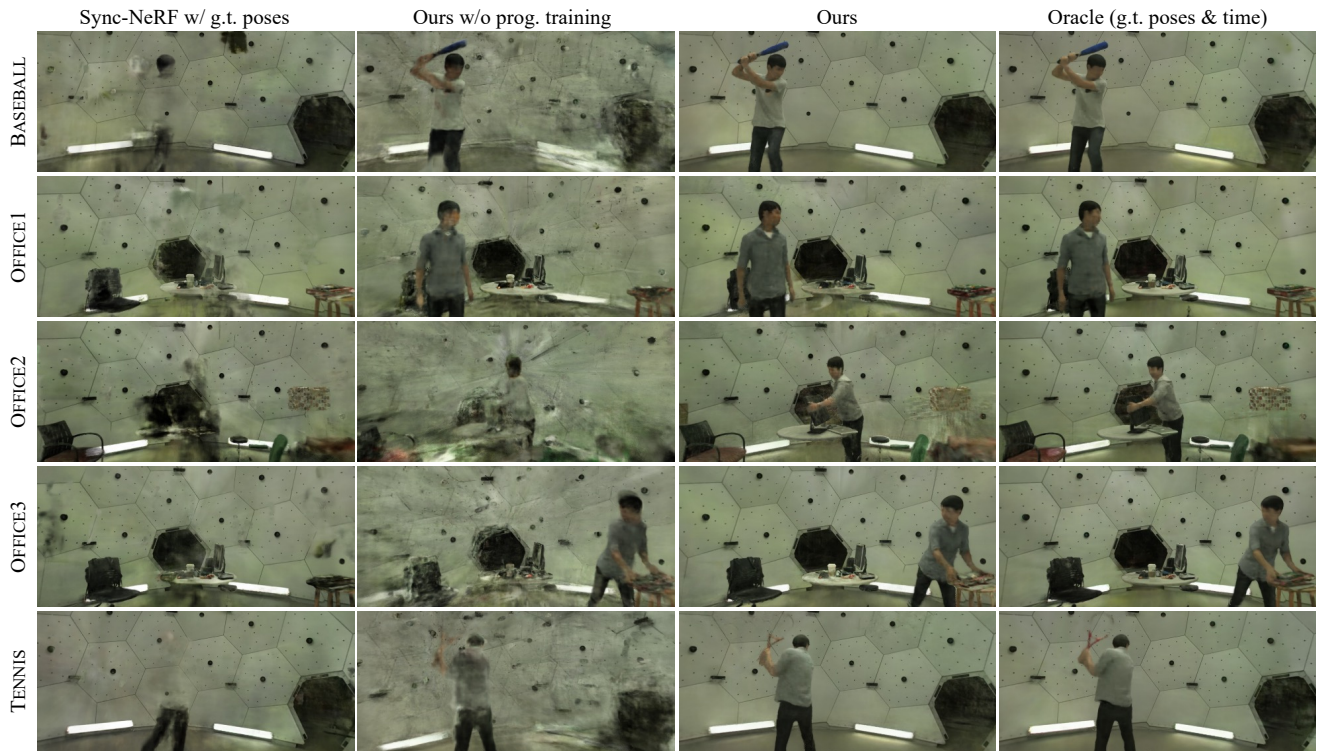


Figure 9. Additional qualitative comparison of novel view synthesis performance.